

Supplementary Information

Diverse π - π stacking motifs modulate electrical conductivity in tetrathiafulvalene-based metal-organic frameworks

Lilia S. Xie,^a Eugeny V. Alexandrov,^{b,c} Grigorii Skorupskii,^a Davide M. Proserpio^{b,d} and Mircea Dincă^{*a}

- a. Department of Chemistry, Massachusetts Institute of Technology, 77 Massachusetts Avenue, Cambridge, Massachusetts 02139, United States
- b. Samara Center for Theoretical Material Science (SCTMS), Samara State Technical University, Molodogvardeyskaya St. 244, Samara, 443100, Russia
- c. SCTMS, Samara University, Moskovskoe shosse 34, 443086, Samara, Russia
- d. Dipartimento di Chimica, Università degli Studi di Milano, Milano, 20133, Italy

*mdinca@mit.edu

Table of Contents

Experimental Methods	S3
Comparative Analysis of Topology	S7
Table S1. Crystal data and structure refinement for 1	S9
Table S2. Crystal data and structure refinement for 2	S10
Table S3. Crystal data and structure refinement for 3	S11
Table S4. Selected S··S contact distances for 1	S12
Table S5. Selected S··S contact distances for 2	S13
Table S6. Selected S··S contact distances for 3	S14
Table S7. Selected TTFTB bond distances for 1	S15
Table S8. Selected TTFTB bond distances for 2	S16
Table S9. Selected TTFTB bond distances for 3	S16
Table S10. Rectangular ligand ratios for TTFTB in 1–3	S16
Figure S1. TTF stacking sequence of 1	S12
Figure S2. TTF stacking sequence of 2	S13
Figure S3. TTF stacking sequence of 3	S14
Figure S4. Thermal ellipsoid plot of 1	S17
Figure S5. Thermal ellipsoid plot of 2	S18
Figure S6. Thermal ellipsoid plot of 3	S19
Figure S7. PXRD patterns of 1	S20
Figure S8. PXRD patterns of 2	S21
Figure S9. PXRD patterns of 3	S22
Figure S10. TGA plots of 1–3	S23
Figure S11. Nitrogen adsorption isotherms of 1–3	S24
Figure S12. Ambient $I-V$ curves of 1–3	S25
Figure S13. Conductivity vs. $(S\cdots S)_{min}$ distance for TTFTB MOFs	S26
Figure S14. Variable temperature $I-V$ curves of 1–3	S27
Figure S15. EPR spectra of 1–3	S28
References	S29

Experimental Methods

Materials. $\text{La}(\text{NO}_3)_3 \cdot 6\text{H}_2\text{O}$ (99.9% REO, Alfa Aesar), *N,N*-dimethylformamide (DMF, 99.9%, EMD Millipore), and ethanol (EtOH, 200 proof, KOPTEC) were obtained from commercial sources and used as received. Tetrathiafulvalene tetrabenzoic acid (H_4TTFTB) was synthesized according to a previously published procedure.¹

Synthesis of $\text{La}_4(\text{HTTFTB})_4$ (1). $\text{La}(\text{NO}_3)_3 \cdot 6\text{H}_2\text{O}$ (5.2 mg, 0.012 mmol) was dissolved in 0.93 mL of 1:1 $\text{H}_2\text{O}/\text{EtOH}$. H_4TTFTB (8.2 mg, 0.012 mmol) was dissolved in 0.47 mL of 3:1 DMF/EtOH. The $\text{La}(\text{NO}_3)_3 \cdot 6\text{H}_2\text{O}$ solution was slowly added to the H_4TTFTB solution in a 2 mL vial. The reaction mixture was heated to 50 °C for 24 hours, affording a dark red polycrystalline powder. The product was washed with 3×2 mL of EtOH. Anal. Calcd. for $\text{La}_4(\text{C}_{34}\text{H}_{17}\text{O}_8\text{S}_4)_4(\text{DMF})(\text{H}_2\text{O})_8 \cdot (\text{H}_2\text{O})_{12}$ ($\text{C}_{139}\text{H}_{115}\text{NLa}_4\text{O}_{53}\text{S}_{16}$): C, 44.93; H, 3.12, N, 0.38. Found: C, 44.82; H, 2.83; N: 0.23. The powder was activated by supercritical CO_2 drying. Calcd. for $\text{La}_4(\text{C}_{34}\text{H}_{17}\text{O}_8\text{S}_4)_4(\text{DMF})(\text{H}_2\text{O})_8$ ($\text{C}_{139}\text{H}_91\text{NLa}_4\text{O}_{41}\text{S}_{16}$): C, 47.70; H, 2.62; N, 0.40. Found: C, 47.51; H, 2.52; N, 0.26.

Synthesis of $\text{La}(\text{HTTFTB})$ (2). $\text{La}(\text{NO}_3)_3 \cdot 6\text{H}_2\text{O}$ (10.9 mg, 0.0252 mmol) was dissolved in 0.70 mL of 1:1 $\text{H}_2\text{O}/\text{EtOH}$. H_4TTFTB (8.6 mg, 0.013 mmol) was dissolved in 0.70 mL of 3:1 DMF/EtOH. The $\text{La}(\text{NO}_3)_3 \cdot 6\text{H}_2\text{O}$ solution was slowly added to the H_4TTFTB solution in a 2 mL vial. The reaction mixture was heated to 60 °C for 72 hours, affording a dark red polycrystalline powder. The product was washed with 3×2 mL of DMF and 3×2 mL of EtOH. Calcd. for $\text{La}(\text{C}_{34}\text{H}_{17}\text{O}_8\text{S}_4)(\text{DMF})_{0.75}(\text{H}_2\text{O})_{1.25} \cdot (\text{H}_2\text{O})_4$ ($\text{C}_{36.25}\text{H}_{33.75}\text{N}_{0.75}\text{LaO}_{14.5}\text{S}_4$): C, 44.47; H, 3.47; N, 1.07. Found: C, 43.93; H: 2.93; N: 1.56. The powder was activated by heating to 220 °C under dynamic vacuum for 24 hours. Calcd. for $\text{La}(\text{C}_{34}\text{H}_{17}\text{O}_8\text{S}_4)(\text{H}_2\text{O})_{1.5}$ ($\text{C}_{34}\text{H}_{20}\text{LaO}_{9.5}\text{S}_4$): C, 48.18; H, 2.38; N, 0.00. Found: C, 48.27; H, 2.45; N, < 0.02.

Synthesis of $\text{La}_4(\text{TTFTB})_3$ (3). $\text{La}(\text{NO}_3)_3 \cdot 6\text{H}_2\text{O}$ (7.8 mg, 0.018 mmol) was dissolved in 0.50 mL of 1:1 $\text{H}_2\text{O}/\text{EtOH}$. H_4TTFTB (11.1 mg, 0.0162 mmol) was dissolved in 0.90 mL of 3:1 DMF/EtOH. The $\text{La}(\text{NO}_3)_3 \cdot 6\text{H}_2\text{O}$ solution was slowly added to the H_4TTFTB solution in a 2 mL vial. The reaction mixture was heated to 65 °C for 72 hours, affording a red polycrystalline powder. The product was washed with 3×2 mL of DMF and 3×2 mL of EtOH. Calcd. for $\text{La}_4(\text{C}_{34}\text{H}_{16}\text{O}_8\text{S}_4)_3(\text{H}_2\text{O})_6 \cdot (\text{H}_2\text{O})_{13}$ ($\text{C}_{102}\text{H}_{86}\text{La}_4\text{O}_{43}\text{S}_{12}$): C, 41.67; H, 2.95; N, 0.00. Found: C, 41.72; H, 2.88; N, < 0.10. The powder was activated by supercritical CO_2 drying. Calcd. for $\text{La}_4(\text{C}_{34}\text{H}_{16}\text{O}_8\text{S}_4)_3(\text{DMF})_{0.5}(\text{EtOH})_3(\text{H}_2\text{O})_{2.5} \cdot (\text{H}_2\text{O})_{0.5}$ ($\text{C}_{109.5}\text{H}_{75.5}\text{N}_{0.5}\text{La}_4\text{O}_{30.5}\text{S}_{12}$): C, 46.53; H, 2.69; N, 0.25. Found: C, 46.22; H, 3.02; N, 0.30.

Activation via supercritical CO_2 drying. The powders were soaked in EtOH for 24 hours with 3 solution changes. The samples were then transferred to a Tousimis Samdri-PVT-3D dryer. The EtOH was exchanged with liquid CO_2 over a period of 30 minutes, alternating 5 minutes of soaking and 5 minutes of venting under a positive pressure of CO_2 . The chamber was then sealed and heated to about 40 °C, reaching a pressure of about

1,300 psi. After 30 minutes above the critical point of CO₂ (31 °C and 1,071 bar), the CO₂ pressure was vented over the course of 8 hours. The products were heated to 50 °C under dynamic vacuum for 8 hours and then stored in an argon-filled glovebox.

Single crystal X-ray diffraction. Solvated, diffraction-quality single crystals were mounted in Paratone oil on Kapton loops. Low temperature (100 K) diffraction data (ρ - and ω -scans) were collected on a Bruker-AXS X8 Kappa Duo diffractometer coupled to a Smart APEX II CCD detector using $I\mu S$ -micro sources of Cu K α radiation ($\lambda = 1.5406 \text{ \AA}$) for **1**, and Mo K α radiation ($\lambda = 0.71073 \text{ \AA}$) for **2** and **3**. Absorption and other corrections were applied using SADABS. The structures were solved by direct methods using SHELXT² and refined against F^2 on all data by full-matrix least squares with SHELXL-2016³ using the ShelXle graphical user interface.⁴ For **1**, due to the data quality and extensive disorder, coordinated solvent molecules could not be resolved; only the oxygen atoms were included in the model. All non-hydrogen atoms were refined anisotropically, with the exception of low-occupancy solvent oxygen atoms coordinated to La. The data quality precluded location of acidic hydrogen atoms on the TTFTB ligand in the electron density map (singly protonated ligands were assigned to obtain a charge-balanced formula). For **2** and **3**, all non-hydrogen atoms were refined anisotropically. All acidic hydrogen atoms on the TTFTB ligand and coordinated water molecules included in the model were located in the electron density maps. For **1**, **2** and **3**, hydrogen atoms on the ligand and resolved DMF molecules were included in the model at geometrically calculated positions and refined using a riding model. Disordered residual electron density contributions in the pores were removed by SQUEEZE⁵ using PLATON.⁶ Details of the refinements, including data quality and a summary of residual values, are listed in Tables S1–S3.

Powder X-ray diffraction. Patterns were collected on a Bruker Advance II diffractometer equipped with $\theta/2\theta$ Bragg-Brentano geometry and Ni-filtered Cu K α radiation ($K\alpha_1 = 1.5406 \text{ \AA}$, $K\alpha_2 = 1.5444 \text{ \AA}$, $K\alpha_1/K\alpha_2 = 0.5$). The tube voltage and current were 40 kV and 40 mA, respectively. Samples were prepared by placing a thin layer of the appropriate material on a zero-background silicon crystal plate.

Thermogravimetric analysis. Using a TA Instruments Q500 Thermogravimetric Analyzer, measurements were carried out on powder samples between 25 and 700 °C at a heating rate of 3 °C/min under a nitrogen gas flow of 35 mL/min on a platinum pan.

Nitrogen adsorption measurements. A Micromeritics ASAP 2020 Surface Area and Porosity Analyzer was used to measure the nitrogen isotherms. An oven-dried sample tube equipped with a TranSeal (Micromeritics) was weighed. The sample was transferred to the tube and evacuated under dynamic vacuum until the outgas rate was less than 2 mTorr/minute. The tube was then filled with nitrogen gas and weighed again, and the sample mass was determined by subtracting the mass of the empty tube and TranSeal. The nitrogen isotherm was measured in a liquid nitrogen bath (77 K). UHP grade nitrogen and oil-free valves and gas regulators were used for all free space corrections and measurements.

Room temperature conductivity measurements. Two-contact probe measurements were carried out at 296 K in ambient atmosphere on pressed pellets using a home-built two-probe in situ press set-up described previously.⁷ Powders were loaded into glass tubes and pressed between stainless steel rods under approximately 200 MPa. Linear I - V curves were obtained by sweeping the voltage between -0.5 to $+0.5$ V or -1 to $+1$ V and measuring the current using a sourcemeter (Keithley 2450) connected to the press via test leads. Pellet thicknesses were measured after the measurement using a micrometer (Mitutoyo). At least two pellets from five separate batches of each phase were measured. For each phase, first, the conductivities of all pellets from each individual batch were averaged to give a batch conductivity value. Then, the batch conductivity values were averaged to give the average conductivity value for the phase. The standard error of the batch conductivity values was used for the error estimation on the average conductivity value for each phase.

Variable temperature conductivity measurements. Two-contact probe measurements were carried out between 250 and 350 K under dynamic vacuum ($\sim 10^{-5}$ Torr) on pressed pellets using a home-built in situ screw cell set-up described previously.⁸ Samples were loaded into Garolite tubes with a threaded inner wall and pressed between two stainless steel screws under approximately 50 MPa. The protruding end of one screw was screwed into a copper mounting chuck to establish thermal and electrical contact with the sample. The chuck was then secured to the platform at the base of a probe station (Janis). Contacts were made by placing the gold-plated tungsten probe tips onto the copper plate and the top screw of the device. The conductance values of the screw cell devices were first measured in ambient atmosphere at 296 K. The chamber was then sealed and evacuated. Once the pressure reached $\sim 10^{-5}$ Torr, the temperature was equilibrated by resistive heating in the probe station base and liquid nitrogen flow, and regulated by a temperature controller (Scientific Instruments 9700). I - V curves were collected by sweeping the voltage from -0.1 to $+0.1$ V or -0.5 to $+0.5$ V upon cooling with a temperature step size of 5 K and 10 minutes per step. The screw cell conductivities were calculated by multiplying the conductance values obtained at each temperature under vacuum by the ratio of the ambient screw cell conductance to the in situ press conductivity of the same batch of material. The activation energy E_a was calculated using the equation $\ln \sigma = \ln \sigma_0 - \frac{E_a}{k_B T}$, where E_a was extracted from the linear least squares fit of $\ln \sigma$ vs. $1/T$. For **3**, due to the low conductance of the sample relative to the noise floor of the sourcemeter, only data between 295 and 350 K were used.

Diffuse reflectance UV-vis-NIR spectroscopy. Spectra were collected between 400 and 2275 nm on a Cary 5000i spectrophotometer at a scan rate of 400 nm/min using a PIKE Technologies DiffusIR accessory. MOF powders were ground with KBr in a mortar and pestle to a 1 wt% dilution. Spectra were normalized to a 100% KBr baseline, and the Kubelka-Munk equation was applied ($F(R) = \frac{(1-R)^2}{2R}$). The Kubelka-Munk function-transformed spectra were then normalized with respect to $F(R)$ at 400 nm ($25,000 \text{ cm}^{-1}$). The Tauc plots were normalized with respect to $[F(R)h\nu]^2$ at 3 eV. The optical band gaps were estimated by a least-squares linear fit within the energy ranges of 2.1–2.5 eV (**1**) and 2.3–2.6 eV (**2** and **3**).

Diffuse reflectance infrared fourier transform spectroscopy (DRIFTS). Spectra were collected on a Bruker Tensor 37 using a PIKE Technologies DiffusIR accessory. MOF powders were ground with KBr in a mortar and pestle to a 1 wt% dilution. Data were averaged over 16 scans between 4200 and 2000 cm^{-1} . Each of the Kubelka-Munk function-transformed DRIFTS spectra were normalized with respect to the DRUV-vis-NIR data by matching the DRIFTS value of $F(R)$ at 4200 cm^{-1} with the DRUV-vis-NIR value of $F(R)$ of the same sample at 4400 cm^{-1} .

Electron paramagnetic resonance spectroscopy. Room temperature X-band measurements were carried out on a Bruker EMX spectrometer equipped with an ER 4199HS cavity and Gunn diode microwave source at room temperature, with a microwave frequency of 9.37 GHz, power of 0.100 mW, and attenuation of 33.0 dB. MOF powders were ground with KBr in a mortar and pestle to a 1 wt% dilution, and measured under a nitrogen atmosphere in septum-sealed quartz tubes.

Comparative Analysis of Topology

We carried out a comparison with 44 rod MOFs of rare earth metals with tetracarboxylate ligands of flat rectangular shape (Spreadsheet S1) and 29 other MOFs with the TTFTB ligand (Spreadsheet S2).

Rods in compounds **1**, **2** and **3** have a wave-like shape with periods of 6, 4, and 4 $\{Ln_2\}$ dimers, respectively. However, topologies of rods in the PE&M representations for the three compounds are different.

The 2,2,4,6C10 motif of the rod in compound **1** is the same as in two compounds $[M_3X_2(NO_3)(DMA)_2(H_2O)] \cdot 5DMA \cdot 2H_2O$ ($M = Y, Dy$; Cambridge Structural Database reference codes OXALOP, OXAMEG) with a tetratopic ligand of flattened tetrahedral shape, tetrakis[4-(carboxyphenyl)oxamethyl]methanoic acid (H_4X).⁹ Curiously, the same rod motif is also observed in 18 other rod MOFs, all with rare earth elements and dicarboxylate ligands (CSD refcodes BALJOQ, DAMYOI, DAMYUO, KEWBUL, KOHWUA, MOTVOI, SABWOK, SABXAX, SABXIF, SABXUR, SABYEC, SABYOM, SABZAZ, SABZIH, WIYWAE, WIYWEI, WIYWOS, WIYWUY).

The rod type of triply-bridged dimers 2,6C1 found in compound **2** is very common for rod MOFs, as it is observed in 375 structures, of which 328 contain rare earths. For example, it is similar to the rod in the compound $[Tb(H_2btcc)_2/4(btcc)_3/6(H_2O)] \cdot 2H_2O$ (MITGUR) with a flat tetratopic ligand of rectangular shape, 1,2,4,5-benzenetetracarboxylic acid (H_4btcc), and observed in other 8 compounds (Spreadsheet S1).¹⁰

The 2,3,6,7-c net of the rod in compound **3** is unique, and to the best of our knowledge, it has never been observed before in rod MOFs.

We extracted the two main features of the TTFTB ligand that lead to the novel topologies: the rectangular ligand ratio (RLR), and the unusual π - π interactions with participation of the sulfur atoms. The RLR is computed from the rectangle of the four carbon atoms from the four carboxylate groups in the tetratopic ligand as the ratio of the average of the two longer sides to the average of the two shorter sides. As was shown before for Zr-MOFs, a less “square” ligand (i.e. with a larger RLR) leads to a reduced connectivity of molecular SBUs, resulting in unusual topologies featuring larger porosity, but less stability.¹¹ For the rod SBUs with rare earth metals, this elongation also influences the topology. Thus, 9,10-dioxo-9,10-dihydroanthracene-1,4,5,8-tetracarboxylate (RLR = 1.1) is coordinated only by two carboxylate groups located on one diagonal, as observed for 6 isorecticular compounds of Er, Dy, Sm, Tb, Eu and Nd.¹² The 1,2,4,5-benzenetetracarboxylate ligand (RLR = 1.6) can be coordinated through two or four carboxylate groups,¹⁰ while 5,5'-diazene-1,2-diyl-diisophthalate (RLR = 1.8)¹³ and 5,5'-(4H-1,2,4-triazole-3,5-diyl)bis(benzene-1,3-dicarboxylate) (RLR = 2.1),¹⁴ similarly to TTFTB in compounds **1** (RLR = 1.7; Table S10), **2** (RLR = 2.1) and **3** (RLR = 1.9) provides all four carboxylate groups for coordination.

In other MOF structures containing TTFTB (Spreadsheet S2), the value of RLR varies in a wide range, from 1.40 to 1.96, that reflects its flexibility in the direction normal to the ligand plane. The 1D column of stacked

ligands is more frequently observed for flattened conformations with larger RLR (> 1.7). In contrast with planar 5,5'-diazene-1,2-diylidiiisophthalate forming continuous columns with an eclipsed configuration of ligands along the rods, the inaccessibility of a flat conformation for the four benzene rings in TTFTB prevents building continuous columns of π - π stacking in an eclipsed configuration in a rod La-MOF, where La-La distances within the rod are in the range of 4.2–5.2 Å. Thus, in the 3D framework Ba(H₂TTFTB)(H₂O)₂ with 1D columns of eclipsed stacks, the TTFTB ligands are separated by 4.124 Å, while the Ba-Ba distances are 4.162 Å within dimers and 6.312 Å between separate dimers.¹⁵

At the same time, the presence of sulfur atoms favors the formation of intermolecular S...S interactions: from the 29 known structures of MOFs with TTFTB extracted from the CSD, 24 have dimers, trimers or 1D columns of interacting ligands (see Spreadsheet S2). The resulting compromise for rod MOFs consists of construction of continuous columns with ligands in the staggered orientation in compound **1**, eclipsed dimers in **2** and slipped-parallel trimers in **3**. Moreover, similarly to compound **1**, four other rod MOFs (CSD refcodes ROYMOJ, ROYMEZ, PEGCIP, ROYMID)^{1,16} show the shortest π ... π contacts (3.27–3.34 Å), responsible for the charge hopping mechanism of conductivity, among the 14 MOFs with TTFTB ligands stacked in 1D staggered columns (Spreadsheet S2). Thus, designing rod MOFs is seen as the most promising for MOF-based semiconducting materials based on this ligand.

Furthermore, the additional structural comparative analysis extracted from the CSD structures of 44 rod MOFs of rare earth metals with tetracarboxylate ligands of flat rectangular shape (Spreadsheet S1) can be useful for screening new electronic semiconductors with tuned topologies, π ... π interactions and conductivity. It should be noted that among 44 rod Ln-MOFs with rectangular ligands, 25 structures contain one-periodic stacks of parallel ligands involved in π ... π interactions, and the shortest contacts between ligands providing one-periodic stacks varies in the range 3.24–3.64 Å, which is similar to the one observed in the structures of compounds **1** and **2** (3.41–4.20 Å). From the data on the topologies of these 25 structures (Spreadsheet S1), we can conclude that three topological types (in PE&M representation) of 3D 3,3,3,3,3,4,5-c new net, 3,4,6T160 and 2D **bex** are favorable for staggered stacks of parallel ligands. The 3D 3,4,6-c new net provides slipped-parallel stacks, and 3D 3,3,3,6-c new net and 3,3,3,3,7T7 can be useful for obtaining an eclipsed arrangement of ligands. However, among the 44 rod Ln-MOFs, only one compound, [Eu₂(btc)(H₂btc)(H₂O)]·4H₂O (H₄btc = 1,2,4,5-benzenetetracarboxylic acid) (MIRLUU), was tested for electrical conductivity, and it was shown to be a semiconductor.¹⁷ The structure of this MOF does not have π ... π interactions, and the authors explain conductivity as a result of the short Eu-Eu distance in rods (3.95 Å).

Table S1. Crystal data and structure refinement for **1**.

Empirical formula	C _{272.5} H _{132.2} La ₈ O ₇₇ S ₃₂ [+ solvent]	
Formula weight	6765.22 g mol ⁻¹	
Temperature	100(2) K	
Wavelength	1.54178 Å	
Crystal system	Orthorhombic	
Space group	Ibam	
Unit cell dimensions	$a = 28.140(3) \text{ \AA}$ $b = 40.411(3) \text{ \AA}$ $c = 83.201(9) \text{ \AA}$	$\alpha = \beta = \gamma = 90^\circ$
Volume	94614(16) Å ³	
Z	8	
Density (calculated)	0.939 g cm ⁻³	
Absorption coefficient	6.882 mm ⁻¹	
<i>F</i> (000)	26480	
Crystal size	0.145 × 0.109 × 0.101 mm ³	
Theta range for data collection	1.062 to 58.930°	
Index ranges	-29 ≤ <i>h</i> ≤ 28, -44 ≤ <i>k</i> ≤ 44, -75 ≤ <i>l</i> ≤ 92	
Reflections collected	142202	
Independent reflections	32569 [<i>R</i> _{int} = 0.0795]	
Completeness to theta = 58.930°	95.0%	
Absorption correction	Semi-empirical from equivalents	
Refinement method	Full-matrix least-squares on <i>F</i> ²	
Data / restraints / parameters	32569 / 2336 / 6491	
Goodness-of-fit on <i>F</i> ²	1.332	
Final <i>R</i> indices [<i>I</i> > 2σ(<i>I</i>)]	<i>R</i> ₁ = 0.1142, <i>wR</i> ₂ = 0.3327	
<i>R</i> indices (all data)	<i>R</i> ₁ = 0.1535, <i>wR</i> ₂ = 0.3654	
Largest diff. peak and hole	2.84 and -2.72 e Å ⁻³	

Table S2. Crystal data and structure refinement for **2**.

Empirical formula	C ₃₇ H ₂₄ LaNO ₉ S ₄ [+ solvent]	
Formula weight	893.72 g mol ⁻¹	
Temperature	100(2) K	
Wavelength	0.71073 Å	
Crystal system	Monoclinic	
Space group	P2 ₁ /c	
Unit cell dimensions	$a = 18.098(4) \text{ \AA}$ $b = 9.345(2) \text{ \AA}$ $c = 22.051(5) \text{ \AA}$	$\alpha = 90^\circ$ $\beta = 90.202(4)^\circ$ $\gamma = 90^\circ$
Volume	3729.6(15) Å ³	
Z	4	
Density (calculated)	1.592 g cm ⁻³	
Absorption coefficient	1.424 mm ⁻¹	
<i>F</i> (000)	1784	
Crystal size	0.005 × 0.04 × 0.09 mm ³	
Theta range for data collection	1.125 to 27.877°	
Index ranges	-16 ≤ <i>h</i> ≤ 23, -12 ≤ <i>k</i> ≤ 10, -29 ≤ <i>l</i> ≤ 29	
Reflections collected	37953	
Independent reflections	8886 [<i>R</i> _{int} = 0.1066]	
Completeness to theta = 25.242°	99.9%	
Absorption correction	Semi-empirical from equivalents	
Refinement method	Full-matrix least-squares on <i>F</i> ²	
Data / restraints / parameters	8886 / 867 / 507	
Goodness-of-fit on <i>F</i> ²	1.005	
Final <i>R</i> indices [<i>I</i> > 2σ(<i>I</i>)]	<i>R</i> ₁ = 0.0484, <i>wR</i> ₂ = 0.1055	
<i>R</i> indices (all data)	<i>R</i> ₁ = 0.0922, <i>wR</i> ₂ = 0.1214	
Largest diff. peak and hole	1.82 and -0.95 e Å ⁻³	

Table S3. Crystal data and structure refinement for **3**.

Empirical formula	C ₅₇ H ₄₀ La ₂ N ₂ O ₁₅ S ₆ [+ solvent]	
Formula weight	1463.09 g mol ⁻¹	
Temperature	100(2) K	
Wavelength	0.71073 Å	
Crystal system	Triclinic	
Space group	P $\bar{1}$	
Unit cell dimensions	$a = 11.099(7)$ Å $b = 14.956(10)$ Å $c = 19.810(8)$ Å	$\alpha = 85.806(15)^\circ$ $\beta = 88.145(16)^\circ$ $\gamma = 86.963(13)^\circ$
Volume	3274(3) Å ³	
<i>Z</i>	2	
Density (calculated)	1.484 g cm ⁻³	
Absorption coefficient	1.540 mm ⁻¹	
<i>F</i> (000)	1452	
Crystal size	0.012 × 0.011 × 0.008 mm ³	
Theta range for data collection	1.367 to 25.026°	
Index ranges	-13 ≤ <i>h</i> ≤ 13, -17 ≤ <i>k</i> ≤ 17, -23 ≤ <i>l</i> ≤ 23	
Reflections collected	31524	
Independent reflections	11165 [<i>R</i> _{int} = 0.1000]	
Completeness to theta = 25.242°	96.4%	
Absorption correction	Semi-empirical from equivalents	
Refinement method	Full-matrix least-squares on <i>F</i> ²	
Data / restraints / parameters	11165 / 1902 / 823	
Goodness-of-fit on <i>F</i> ²	0.993	
Final <i>R</i> indices [<i>I</i> > 2σ(<i>I</i>)]	<i>R</i> ₁ = 0.0673, <i>wR</i> ₂ = 0.1557	
<i>R</i> indices (all data)	<i>R</i> ₁ = 0.1322, <i>wR</i> ₂ = 0.1863	
Largest diff. peak and hole	1.33 and -1.17 e Å ⁻³	

Table S4. Selected S...S contact distances for **1**.

S...S contact	Distance (Å)
S1_1(a)···S3_2	3.650(9)
S2_1(a)···S1_2	3.601(9)
S3_1(a)···S4_2	3.767(9)
S4_1(a)···S2_2	3.746(6)
S1_2···S2_3	3.695(9)
S2_2···S4_3	3.447(6)
S3_2···S1_3	3.762(9)
S4_2···S3_3	3.664(9)
S1_3···S4_4	3.613(4)
S2_3···S2_4	3.715(4)
S3_3···S3_4	3.603(4)
S4_3···S1_4	3.581(4)
S1_4···S1_1(b)	3.892(4)
S1_4···S3_1(b)	3.650(4)
S2_4···S2_1(b)	3.790(4)
S2_4···S4_1(b)	3.640(4)
S3_4···S3_1(b)	3.666(4)
S4_4···S4_1(b)	3.890(4)

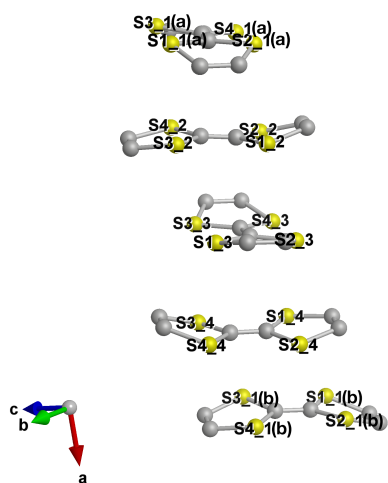


Figure S1. TTF stacking sequence of **1** with S atoms labeled.

Table S5. Selected S...S contact distances for **2**.

S...S contact	Distance (Å)
S1(a)...S4(b)	3.897(3)
S2(a)...S3(b)	3.789(3)
S3(a)...S4(b)	4.525(2)
S1(b)...S2(c)	5.208(3)
S2(b)...S2(c)	4.083(3)

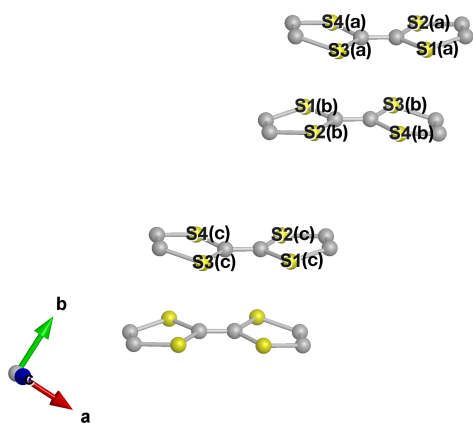


Figure S2. TTF stacking sequence of **2** with S atoms labeled.

Table S6. Selected S...S contact distances for **3**.

S...S contact	Distance (Å)
S1(a)...S6(c)	4.174(6)
S2(a)...S5(c)	4.165(6)
S3(a)...S5(d)	4.164(7)
S3(a)...S6(c)	3.809(6)
S4(a)...S5(c)	3.859(6)
S4(a)...S6(d)	4.140(7)
S1(a)...S4(b)	7.600(8)
S2(a)...S3(b)	7.650(8)
S2(a)...S4(b)	7.072(8)

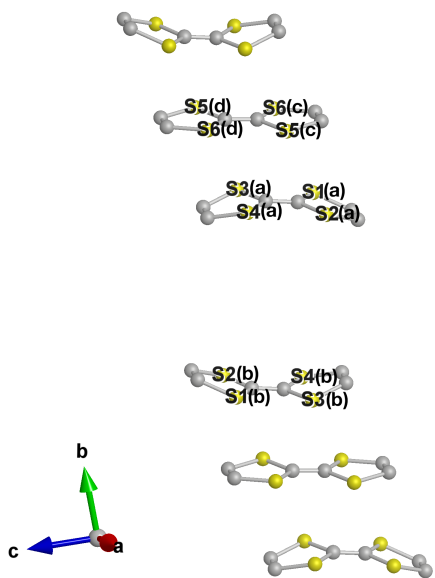


Figure S3. TTF stacking sequence of **3** with S atoms labeled.

Table S7. Selected TTFTB bond distances for **1**.

Bond	Distance (Å)
C1_1–C2_1	1.33(1)
C1_1–S1_1	1.743(9)
C1_1–S2_1	1.75(1)
C2_1–S3_1	1.76(1)
C2_1–S4_1	1.757(9)
C1_2–C2_2	1.27(3)
C1_2–S1_2	1.76(2)
C1_2–S2_2	1.77(2)
C2_2–S3_2	1.78(2)
C2_2–S4_2	1.74(2)
C1_3–C2_3	1.35(2)
C1_3–S1_3	1.75(1)
C1_3–S2_3	1.75(1)
C2_3–S3_3	1.74(1)
C2_3–S4_3	1.77(1)
C1_4–C2_4	1.31(1)
C1_4–S1_4	1.767(9)
C1_4–S2_4	1.76(1)
C2_4–S3_4	1.75(1)
C2_4–S4_4	1.762(9)

Table S8. Selected TTFTB bond distances for **2**.

Bond	Distance (Å)
C1–C2	1.321(7)
C1–S1	1.751(5)
C1–S2	1.761(5)
C2–S3	1.761(5)
C2–S4	1.758(5)

Table S9. Selected TTFTB bond distances for **3**.

Bond	Distance (Å)
C1–C2	1.34(1)
C1–S1	1.73(1)
C1–S2	1.69(1)
C2–S3	1.72(1)
C2–S4	1.76(1)
C7–C7'	1.35(2)
C7–S5	1.74(1)
C7–S6	1.74(1)

Table S10. Values of long and short apertures and their ratio for TTFTB in **1–3**.

Phase	Average of short sides (Å)	Average of long sides (Å)	RLR
1	8.85	14.99	1.70
2	7.68	15.88	2.07
3	8.33	15.49	1.86
Mean value	8.29	15.45	1.88

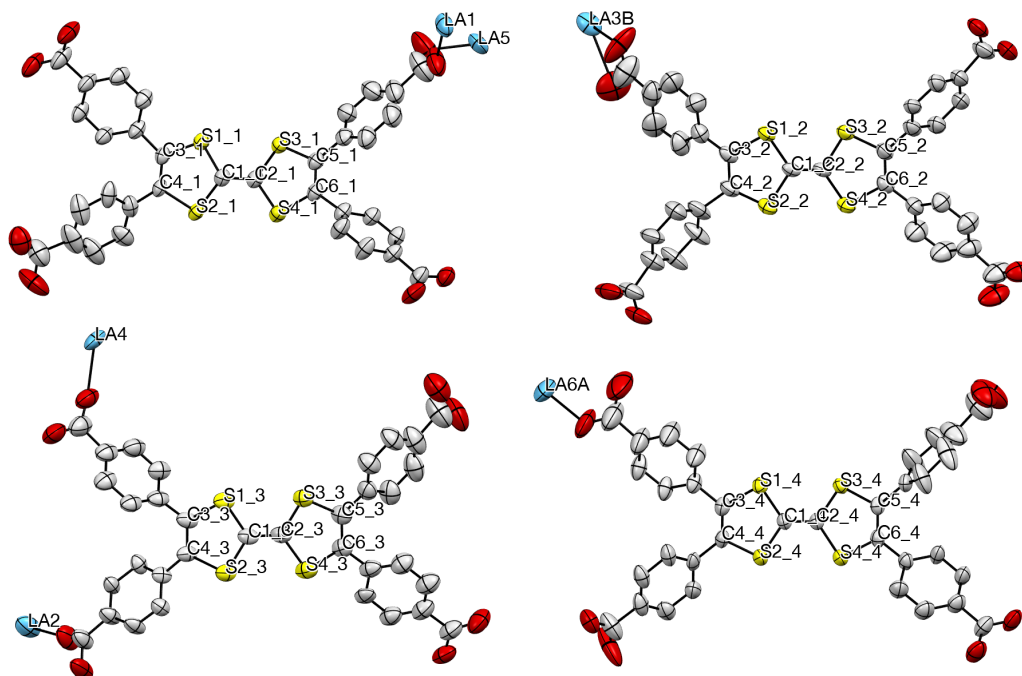


Figure S4. Thermal ellipsoid plots of each TTFTB ligand in the asymmetric unit of **1** drawn at the 50% probability level. Hydrogen atoms, solvents, and minor components of the disorder in the ligand benzoates and La atoms have been omitted for clarity.

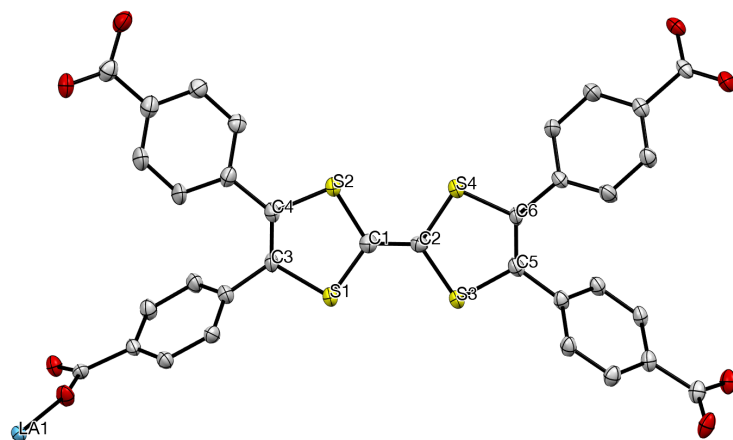


Figure S5. Thermal ellipsoid plot of the asymmetric unit of **2** drawn at the 50% probability level. Hydrogen atoms and solvent molecules have been omitted for clarity.

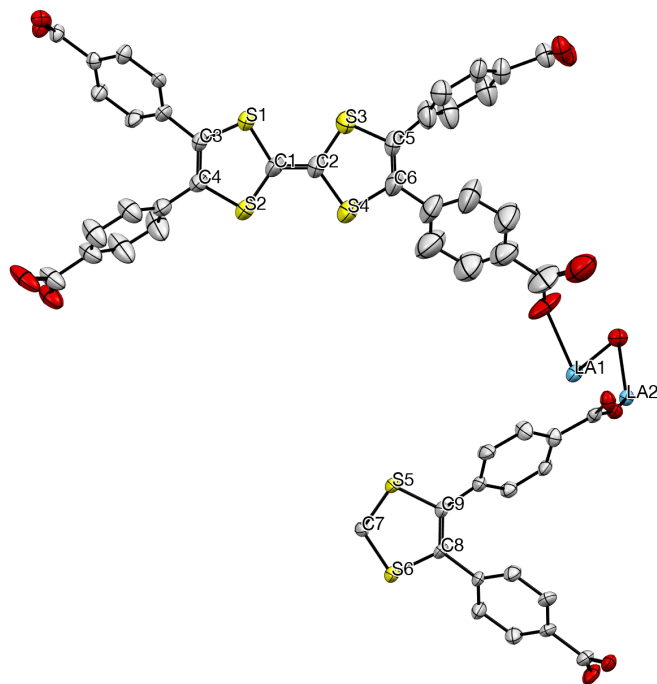


Figure S6. Thermal ellipsoid plot of the asymmetric unit of **3** drawn at the 50% probability level. Hydrogen atoms and solvent molecules have been omitted for clarity.

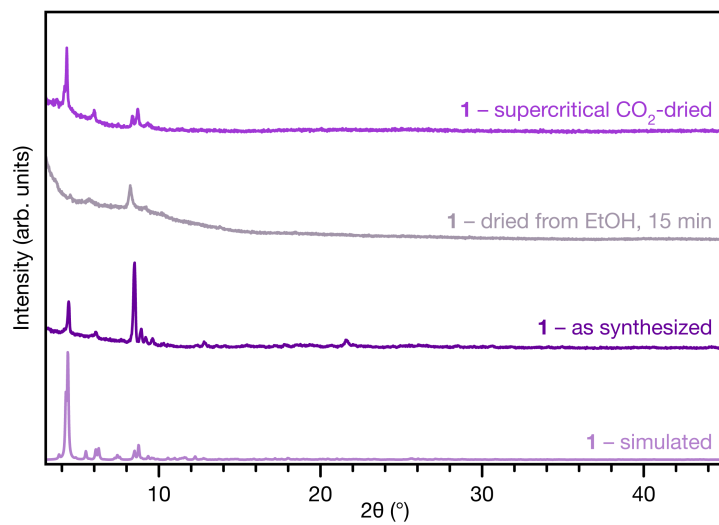


Figure S7. Experimental powder X-ray diffraction patterns of **1** as synthesized, dried, and activated via supercritical CO₂ drying, compared to the simulated pattern from the single crystal structure of **1**.

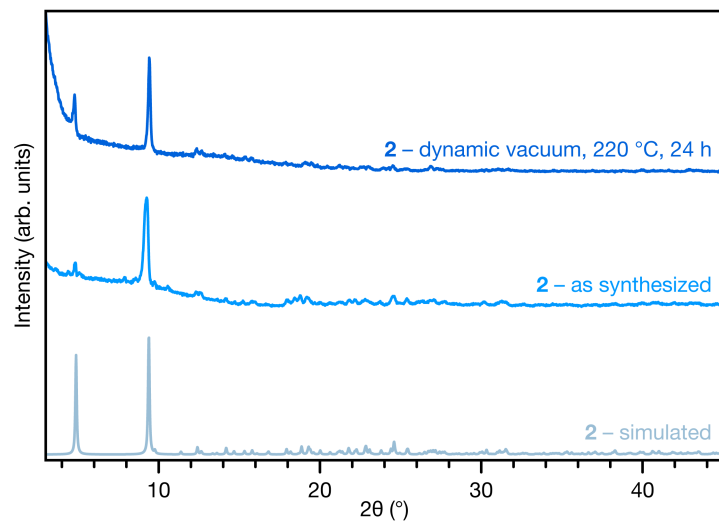


Figure S8. Experimental powder X-ray diffraction patterns of **2** as synthesized and activated under vacuum, compared to the simulated pattern from the single crystal structure of **2**.

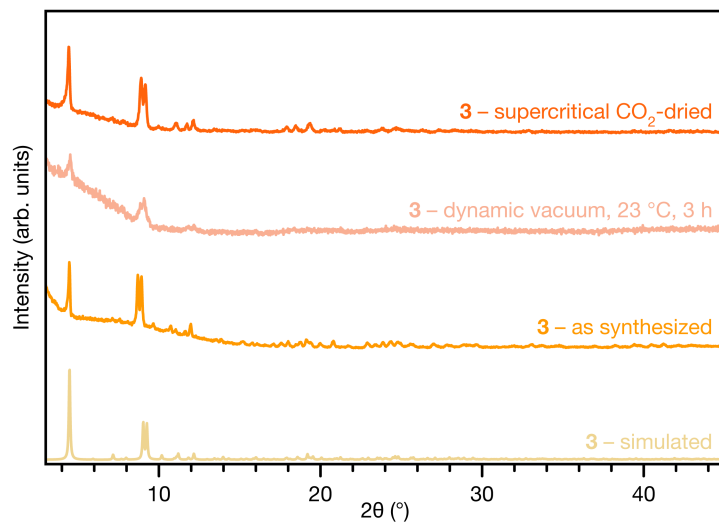


Figure S9. Experimental powder X-ray diffraction patterns of **3** as synthesized, activated under vacuum, and activated via supercritical CO₂ drying, compared to the simulated pattern from the single crystal structure of **3**.

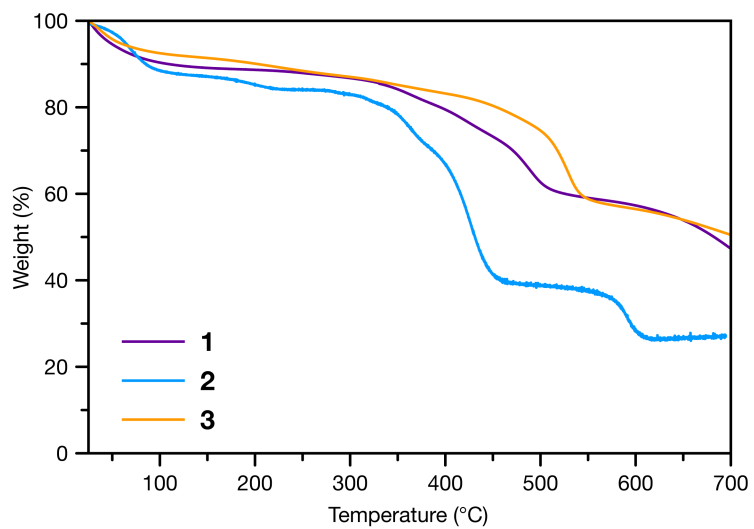


Figure S10. Thermogravimetric analysis plots for **1**, **2**, and **3**.

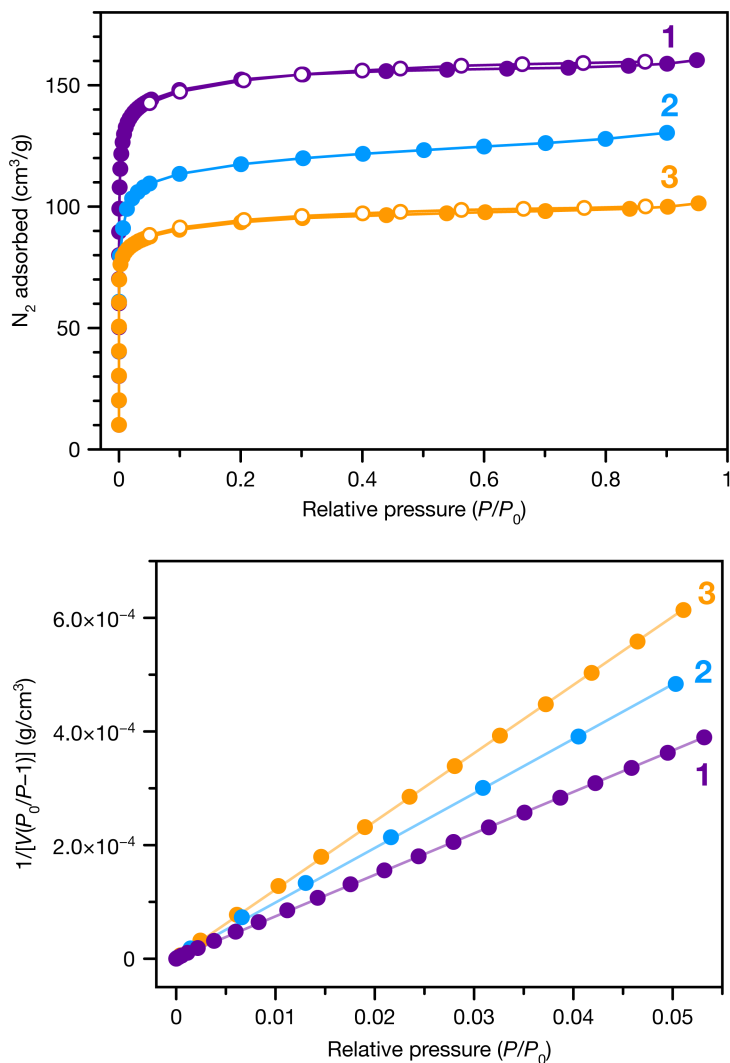


Figure S11. Upper panel: Nitrogen adsorption isotherms for **1**, **2**, and **3** at 77 K. Closed circles correspond to adsorption and open circles correspond to desorption. Lower panel: portions of the isotherms satisfying the Brunauer–Emmett–Teller (BET) consistency criteria;^{18,19} closed circles indicate the BET function-transformed data, and the solid lines correspond to a linear fit to the data.

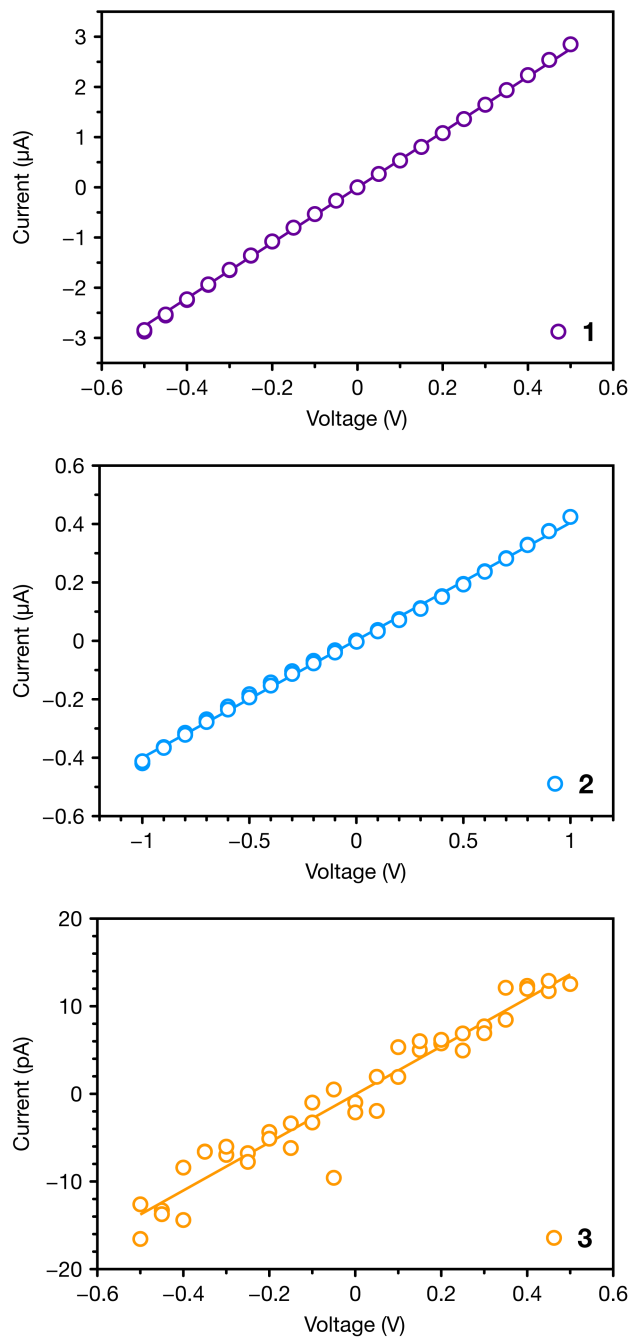


Figure S12. Representative I - V curves at 296 K for two-contact probe pressed pellet devices of **1**, **2**, and **3**. The solid lines correspond to linear fits to the data.

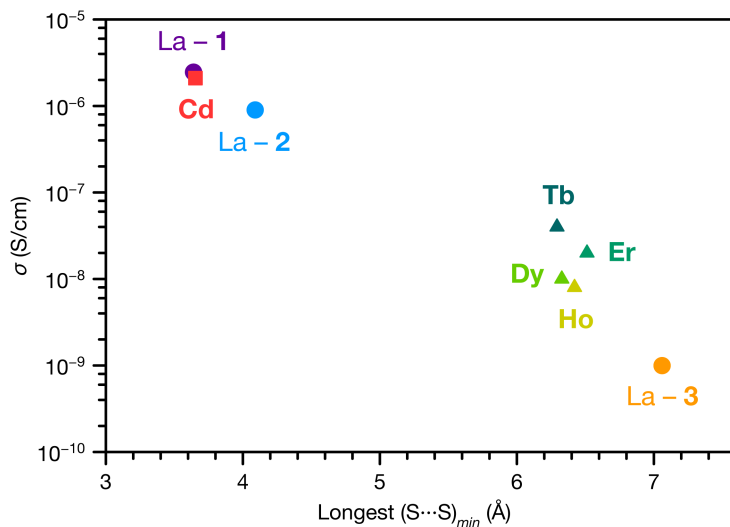


Figure S13. Two-contact probe pressed pellet conductivities for TTFTB MOFs with 1D ligand stacking motifs vs. the longest $(S\cdots S)_{min}$ contact distance (i.e. the longest S...S distance found between all pairs of nearest neighbor TTFTB pairs in their crystal structures). La - 1, La - 2, and La - 3 correspond to the phases reported in this work. Cd corresponds to $Cd_2(TTFTB)$.⁷ Tb, Dy, Ho, and Er correspond to the frameworks with the indicated lanthanide before I₂ treatment.²⁰

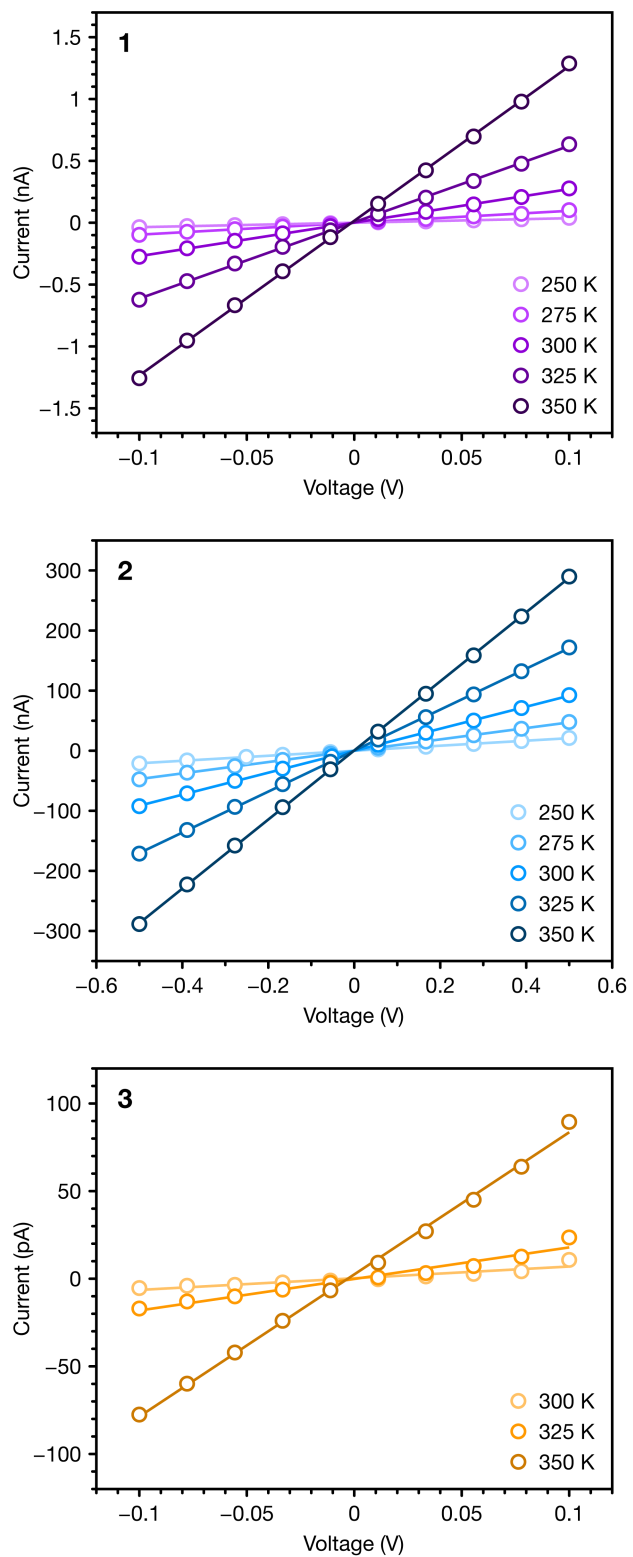


Figure S14. I - V curves at different temperatures for two-contact probe pressed pellet devices of **1**, **2** and **3**. The solid lines correspond to linear fits to the data.

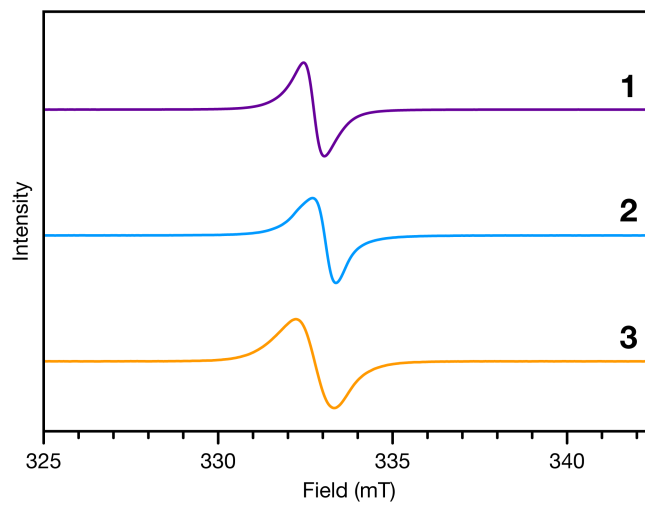


Figure S15. X-band electron paramagnetic resonance spectra of **1**, **2** and **3**. The signals correspond to $g = 2.012$ for **1** and **3**, and $g = 2.011$ for **2**.

References

- 1 T. C. Narayan, T. Miyakai, S. Seki and M. Dincă, *J. Am. Chem. Soc.*, 2012, **134**, 12932–12935.
- 2 G. M. Sheldrick, *Acta Cryst.*, 2014, **A71**, 3–8.
- 3 G. M. Sheldrick, *Acta Cryst.*, 2015, **C71**, 3–8.
- 4 C. B. Hübschle, G. M. Sheldrick and B. Dittrich, *J. Appl. Cryst.*, 2011, **44**, 1281–1284.
- 5 P. van der Sluis and A. L. Spek, *Acta Cryst.*, 1990, **A46**, 194–201.
- 6 A. L. Spek, *Acta Cryst.*, 2009, **D65**, 148–155.
- 7 L. Sun, S. S. Park, D. Sheberla and M. Dincă, *J. Am. Chem. Soc.*, 2016, **138**, 14772–14782.
- 8 L. Sun, C. H. Hendon, S. S. Park, Y. Tulchinsky, R. Wan, F. Wang, A. Walsh and M. Dincă, *Chem. Sci.*, 2017, **8**, 4450–4457.
- 9 T. F. Liu, J. Lü, C. Tian, M. Cao, Z. Lin and R. Cao, *Inorg. Chem.*, 2011, **50**, 2264–2271.
- 10 R. Cao, D. Sun, Y. Liang, M. Hong, K. Tatsumi and Q. Shi, *Inorg. Chem.*, 2002, **41**, 2087–2094.
- 11 H. Wang, X. Dong, J. Lin, S. J. Teat, S. Jensen, J. Cure, E. V. Alexandrov, Q. Xia, K. Tan, Q. Wang, D. H. Olson, D. M. Proserpio, Y. J. Chabal, T. Thonhauser, J. Sun, Y. Han and J. Li, *Nat. Commun.*, 2018, **9**, 1745.
- 12 W. H. Yan, S. S. Bao, L. L. Ding, C. S. Lu, Q. J. Meng and L. M. Zheng, *Inorg. Chem. Commun.*, 2013, **28**, 20–24.
- 13 S. Zhang, E. Duan and P. Cheng, *J. Mater. Chem. A*, 2015, **3**, 7157–7162.
- 14 J.-J. Lin, Z. Liu, L.-Z. Lv and Y.-L. Feng, *Chin. J. Inorg. Chem.*, 2018, **34**, 230–236.
- 15 B. Chen, Z.-P. Lv, C. F. Leong, Y. Zhao, D. M. D'Alessandro and J.-L. Zuo, *Cryst. Growth Des.*, 2015, **15**, 1861–1870.
- 16 S. S. Park, E. R. Hontz, L. Sun, C. H. Hendon, A. Walsh, T. Van Voorhis and M. Dincă, *J. Am. Chem. Soc.*, 2015, **137**, 1774–1777.
- 17 C.-D. Wu, C.-Z. Lu, W.-B. Yang, S.-F. Lu, H.-H. Zhuang and J.-S. Huang, *Eur. J. Inorg. Chem.*, 2002, **2002**, 797–800.
- 18 J. Rouquerol, F. Rouquerol, P. Llewellyn, G. Maurin and K. S. W. Sing, *Adsorption by Powders and Porous Solids: Principles, Methodology and Applications*, Academic Press, London, 2013.
- 19 T. C. Wang, W. Bury, D. A. Gómez-Gualdrón, N. A. Vermeulen, J. E. Mondloch, P. Deria, K. Zhang, P. Z. Moghadam, A. A. Sarjeant, R. Q. Snurr, J. F. Stoddart, J. T. Hupp and O. K. Farha, *J. Am. Chem. Soc.*, 2015, **137**, 3585–3591.
- 20 J. Su, T. H. Hu, R. Murase, H. Y. Wang, D. M. D'Alessandro, M. Kurmoo and J. L. Zuo, *Inorg. Chem.*, 2019, **58**, 3698–3706.